Original Paper

Numerical and physical simulations of array laterolog in deviated anisotropic formation

Yi-Zhi Wu [a, b, c], Zhen-Guan Wu [a, b, c], Yi-Ren Fan [a, b, c, *], Tao Xing [a, b, c], Chao-Liu Li [d], Chao Yuan [d]

[a] School of Geosciences, China University of Petroleum, Qingdao, 266580, Shandong, China
[b] Laboratory for Marine Mineral Resources, Qingdao National Laboratory for Marine Science and Technology, Qingdao, 266071, Shandong, China
[c] CNPC Key Laboratory for Well Logging, China University of Petroleum, Qingdao, 266580, Shandong, China
[d] Research Institute of Petroleum Exploration and Development, PetroChina, Beijing, 100083, China

ARTICLE INFO

ABSTRACT

Due to the tremendous amount of high-resolution measurement information, array laterolog is widely used in evaluations of deviated anisotropic reservoirs. However, the precision of a complementary numerical simulation should be improved as high as the core of fine-scale reservoir evaluation. Therefore, the 3D finite element method (3D-FEM) is presented to simulate the array laterolog responses. Notably, a downscaled physical simulation system is introduced to validate and calibrate the precision of the 3D-FEM. First, the size of the downscaled system is determined by *COMSOL*. Then, the surrounding and investigated beds are represented by a sodium chloride solution and planks soaked in solution, respectively. Finally, a half-space measurement scheme is presented to improve the experimental efficiency. Moreover, the corresponding sensitivity function and separation factor are established to analyze the effects of the formation anisotropy and dipping angle on the array laterolog responses. The numerical and experimental results indicate that the half-space method is practical, and the mean relative error between the numerical and experimental results is less than 5%, which indicates that the numerical simulation is accurate. With the proposed approach, the reversal angle of array laterolog response curves in anisotropic formations can be observed, and this range is determined to be $50°-62°$.

1. Introduction

High-angle/horizontal well technology is widely used for hydrocarbon development in unconventional reservoirs, e.g., carbonates and shales (Frenkel et al., 2000; Jiang et al., 2010; Hu et al., 2017). In tight reservoirs, electric anisotropy can be observed due to the presence of stratigraphic fractures, particles of different shapes, and thin interbedded layers, which make it difficult to identify and evaluate hydrocarbon-bearing formations (Deng et al., 2006; Xia et al., 2011; Hu and Fan, 2018; Wu et al., 2019a; Fan et al., 2019). Due to the abundance of measurements that can be obtained and the strong focusing ability of the array laterolog technology developed by Schlumberger in 1998, it is commonly applied for

reservoir identification and fine-scale interpretation (Itskovich et al., 1998; Wang et al., 1999; Yuan et al., 2020). Therefore, an accurate forward-modeling method inspired by the array laterolog is urgently needed for the processing of logging data (Griffiths et al., 2000; Maurer et al., 2009; Yin et al., 2014; Wu et al., 2020). The finite difference method and finite element method were used to address the 2D problem associated with borehole and mud invasion in vertical wells (Ollivier et al., 2002; Chen, 2009; Deng et al., 2010; Jadwiga et al., 2016; Wu et al., 2019b). However, 3D simulations of high-angle/horizontal wells in anisotropic formations are needed to further interpret array laterolog responses (Isabelle et al., 2017). To solve this problem, the 3D finite element method (3D-FEM) was introduced to consider the dipping angle, invasion and anisotropy (Attila et al., 2016; Li and Wang, 2019). To date, forward-modeling methods for predicting array laterolog responses have been extensively investigated. However, physical simulations have not been discussed but are important for validating numerical simulation algorithms.

* Corresponding author. School of Geosciences, China University of Petroleum, Qingdao, 266580, Shandong, China.
E-mail address: fanyiren@upc.edu.cn (Y.-R. Fan).

Physical simulations are generally used to calibrate and analyze the detection performance of laterolog-type instruments (Yuan et al., 2018). However, array laterolog experiments in deviated anisotropic formations have rarely been studied due to technique and model design constraints. Twenty years ago, the Sichuan Petroleum Administration, a company that performs logging activities, conducted physical studies of the dual laterolog responses in fractured formations with various relative angles between the fracture and background bed (Zhao and Bu, 1994). The first downscaled laboratory formation model was established based on electromagnetic field theory, and the resulting laboratory experiments verified the correctness of the numerical algorithm and the stable performance of dual laterolog instrumentation (Ke et al., 1996, 2003). Recently, a downscaled physical laboratory simulation platform was designed based on the FEM (Fan et al., 2016). Furthermore, an improved method was developed to analyze the response characteristics of dual laterolog in cave-type reservoirs. In addition, a new analytical method was presented to perform downscaled physical simulations of well-intersecting fractures (Ge et al., 2019). Typically, almost all physical simulations have focused on the dual laterolog, and on vertical wells in inhomogeneous media. Therefore, a deviated anisotropic formation model must urgently be developed based on the appropriate technology.

In this paper, numerical and physical simulations are combined to analyze the response characteristics of array laterolog in deviated anisotropic formations. Based on 3D-FEM modeling, the sizes of the downscaled instrument and anisotropic formation model are determined. Then, conductive media are designed to simulate an anisotropic formation model. In this approach, the physical simulation of array laterolog responses can be performed in various models with different relative dipping angles between the formation boundary and well trajectory. Finally, the effects of anisotropy and the dipping angle on the array laterolog responses are analyzed, and the range of reversal angles is determined.

2. Forward modeling method

In this paper, the high-resolution laterolog array (HRLA) instrument (Smits et al., 1998) developed by Schlumberger is introduced. Fig. 1 shows the instrument configuration for the HRLA, which consists of a main electrode A0, six pairs of shielding electrodes A1-A6 (A1′-A6′), and two pairs of monitoring electrodes M1 and M2 (M1′ and M2′).

The current injected from the main electrode is focused by the adjacent shielding electrodes and then flows into the formation. By changing the transceiver combinations, 6 kinds of apparent resistivity curves with different depths of investigation (*DoIs*) can be obtained, denoted as *RLA0−RLA6*.

The forward-modeling problem can be transformed into an extreme functional problem based on the 3D-FEM (Zhang, 2009):

$$\varphi(U) = \frac{1}{2}\iiint_\Lambda \frac{1}{\rho}\left[\left(\frac{\partial U}{\partial r}\right)^2 + \frac{1}{r^2}\left(\frac{\partial U}{\partial \varphi}\right)^2 + \left(\frac{\partial U}{\partial z}\right)^2\right]\mathrm{d}\Lambda - \sum_{i=0}^{6} I_i U_i \tag{1}$$

where Λ is the solution area and I_i and U_i are the current and potential of each electrode, respectively.

Furthermore, Dirichlet and Neumann boundary conditions must be satisfied at the outer boundary and the surface of the insulated electrode:

$$U|_{\Gamma_1} = 0;\frac{\partial U}{\partial \overrightarrow{n}}\bigg|_{\Gamma_2} = 0 \tag{2}$$

where Γ_1 and Γ_2 represent the outer boundary and the surface of the insulated electrode, respectively.

On the surfaces of the main electrode and shielded electrodes, the equipotential boundary conditions should be satisfied:

$$-\iint_{\Gamma_3}\frac{1}{\rho}\frac{\partial U_{A_i}}{\partial \overrightarrow{n}}\mathrm{d}S = I_i \tag{3}$$

where U_{A_i} is the potential of electrode A_i, ρ is the resistivity of the region where electrode A_i is located, Γ_3 is the surface of the main or shielded electrode, $\overrightarrow{n}$ is the unit normal vector at the interface of A_i and I_i is the emission current intensity.

The 3D-FEM is adopted to discretize the solution area and set the derivative of φ with respect to U equal to zero:

$$\frac{\partial \varphi}{\partial U} = K\tilde{U} - f = 0 \tag{4}$$

where K is the stiffness matrix.

The electric field generated by any transmitting electrode in the formation can be obtained by solving the above sparse linear equations.

3. Physics simulation system of array laterolog

3.1. Physical simulation system composition

The physical simulation system for the studied array laterolog mainly includes a downscaled instrument module, a downscaled formation module, a measuring module and a postprocessing module, as shown in Fig. 2(a). The formation module is mainly composed of two isotropic surrounding beds and one anisotropic bed. In the laboratory, the surrounding beds are designed based on sodium chloride solution with an adjustable resistivity range of 2−2000 Ω m. The anisotropic bed is composed of a layered solid wood medium saturated with sodium chloride solution, and the resistivity of this medium can be adjusted by changing the concentration of sodium chloride in the solution. The horizontal and vertical resistivities of the bed range from 5 Ω m to 100 Ω m and 10 Ω m to 500 Ω m, respectively. The measuring module mainly contains a stepping motor, oscilloscope, circuit and operation system (OS). The system works as follows: (1) The downscaled instrument is calibrated in a homogeneous formation; (2) the instrument is moved by the stepping motor controlled by the OS to ensure that point-by-point and uniform velocity measurements are obtained; and (3) measurements are collected and input into the computer terminal for graphic display in real time. Fig. 2(b) shows the details of the physical simulation system in the laboratory.
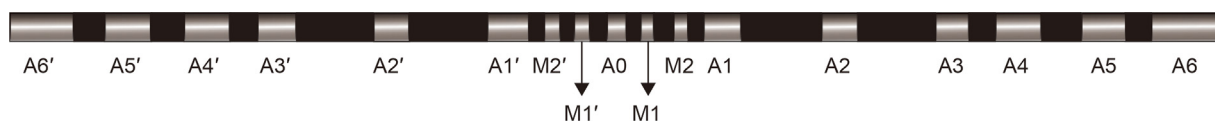

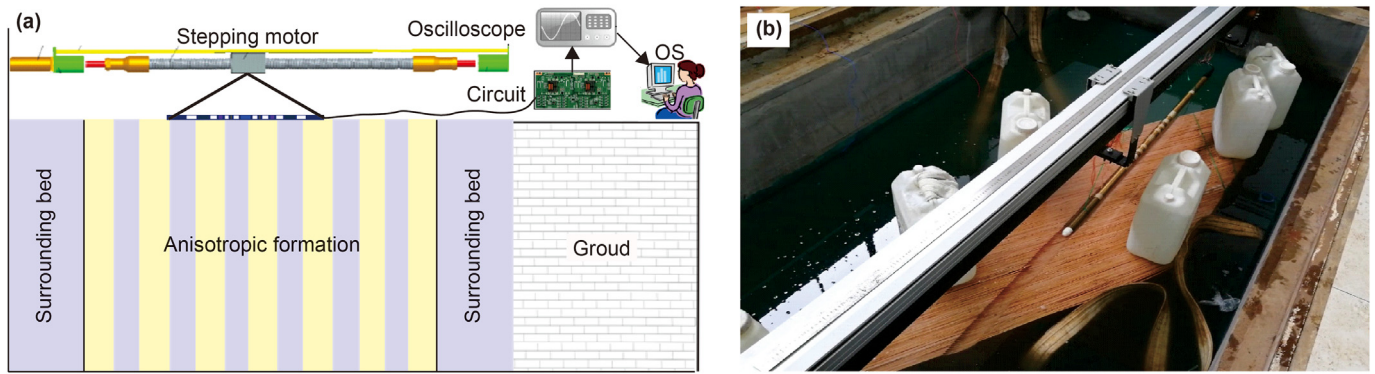**Fig. 1.** Instrument configuration for the HRLA.

Fig. 2. System used for physical simulation of the array laterolog: (a) physical simulation system composition; (b) physical simulation platform in the laboratory.

3.2. Downscaled size of the instrument and formation module

Two conditions must be considered when establishing the physical simulation system: (1) reconstructing the subsurface environment as accurately as possible and (2) creating a feasible and convenient environment for performing operations. Therefore, the core objective of physical simulations is to determine the size of the downscaled instrument and formation model and guarantee that the detection performance of the instrument is similar to that of traditional instruments. In this section, the truncated boundaries and the effects of the downscaling ratio on the electric field generated by the HRLA are considered to determine the size of the downscaled instrument and formation module.

Since the lateral size of the HRLA does not affect the detection performance, the lateral size is designed to be 5 cm based on laboratory manufacturing technology; i.e., the lateral downscaling ratio SR_{lat} is 1/3. The longitudinal size mainly depends on the primary emitting electrode, and the minimum size is fixed at 0.5 cm, i.e., the longitudinal downscaling ratio SR_{lon} is 1/6. Fig. 3 displays the structure of the downscaled HRLA tool. The radius of this instrument is 5 cm. The length is 1.49 m, of which the length of the monitoring electrode is up to 5 cm. The structure of the downscaled instrument is the same as that of the original HRLA, and the electrode sizes for the original and downscaled instruments are given in Table 1. Notably, the return electrodes at both ends of the HRLA can be shortened to optimize the length of

the downscaled instrument.

Furthermore, to investigate the influence of the downscaling scheme on the electric field and determine the size of the formation model, the truncated boundaries are applied to the electric field generated by the downscaled instrument, and the results are compared with the equivalent downscaled instrument (both SR_{lat} and SR_{lon} are 1/6) without truncated boundaries based on the physical simulation software COMSOL. Fig. 4(a)-(e) illustrates the five electric fields, namely, E_{RLA1}–E_{RLA5}, generated with the equivalent downscaling scheme. Fig. 4(f)–(j) shows the five electric fields, namely, $E_{RLA1'}$–$E_{RLA5'}$, generated by the downscaling scheme without truncated boundaries. In detail, the DoI gradually increases in enhanced detection mode, and the maximum DoI is less than 1 m. Moreover, because the measurement point is far from the center of the main electrode of the instrument, the minimum potential can be 0. All the results indicate that the electric fields generated by the two schemes are basically the same. The borehole diameter, mud resistivity and formation resistivity are set to 6 cm, 0.1 Ω m and 100 Ω m, respectively. The full-size horizontal and vertical truncated boundaries are 2.0 m and 4.0 m, respectively.

It can be concluded that the five electric fields generated by the two instruments are almost consistent, which indicates that the downscaling scheme is feasible (1/3 laterally and 1/6 longitudinally). Additionally, the length, width and height of the downscaled formation module can be set to 4.0 m, 2.0 m and 2.0 m, respectively, considering the truncated boundaries.
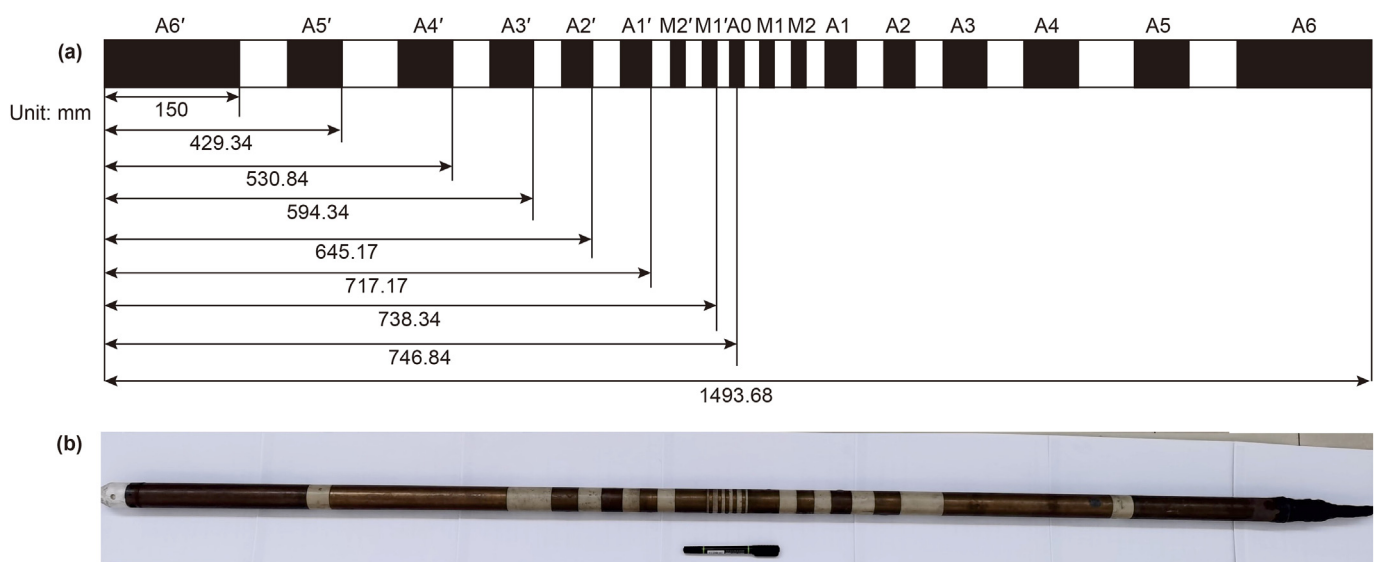

Fig. 3. (a) Structure of the downscaled HRLA experimental tool; (b) actual downscaled HRLA tool.

Table 1
Electrode system structure.

Electrode	A0	M1	M2	A1	A2	A3	A4	A5	A6
Original size, mm	30	30	30	279	152	178	228	1486	3048
Downscaled size, mm	5	5	5	46.5	25.33	29.67	38	247.67	150

In addition, the *DoIs* of these two instruments are calculated based on pseudo-geometric factor theory to assess their detection performance, as shown in Fig. 5. The pseudo-geometry factor is expressed as (Zhu et al., 2019)

$$GF = (R_t - Ra) / (R_t - R_{xo}) \tag{5}$$

where R_t and R_{xo} are the resistivities of virgin and invaded formations, respectively, and Ra is the apparent resistivity.

Fifty percent of the pseudo-geometric factor is defined as the *DoI*. In Fig. 5, the *DoIs* of the original instrument *RLA_or* are all larger than those of the downscaled instrument *RLA_sd*. The maximum *DoIs* of these two instruments are 0.732 and 0.12, respectively, suggesting that the downscaled instrument meets the relevant experimental requirements.

3.3. Anisotropic formation model design

3.3.1. Design method

A thinly interbedded model is designed to represent anisotropic formations. As shown in Fig. 6(a), the model includes two media. The thicknesses of the media are l_1 and l_2. The resistivities are R_1 and R_2. The horizontal resistivity of the model can be expressed as

$$R_h = \frac{(l_1 + l_2)R_1 R_2}{R_2 l_1 + R_1 l_2} \tag{6}$$

The anisotropic coefficient is

$$\lambda = \left(\frac{R_v}{R_h}\right)^{1/2} = \left[1 + R_1 R_2 \left(\frac{1}{R_1} - \frac{1}{R_2}\right)^2 \frac{l_1 l_2}{(l_1 + l_2)^2}\right]^{1/2} \tag{7}$$

where R_v and R_h are the vertical and horizontal resistivities, respectively, and λ is the anisotropy coefficient.

From Eq. (7) and Fig. 6(b), formation models with different anisotropy coefficients can be constructed by changing the resistivity (R_1 or R_2) and relative thickness of the thin interbeds (l_2/l_1). In this paper, the saturated sodium chloride solution and saturated wood are used to represent the two media in the model. For the selection of wood material, through comparative analysis of 3 mm linden board, 3 mm balsa board, 1 mm balsa board, 1 mm cork board, 3 mm populus board and 1 mm populus board saturated with solution (the value here represents the thickness of the board), it is finally determined that 3 mm linden board is best suited as equivalent to the intermediate material. However, considering the scope of this paper, the details of the comparative analysis will not be mentioned. To explore the stability of the anisotropic resistivity of the final determined equivalent medium, Fig. 7(a) shows that the horizontal and vertical resistivities of the model vary with saturation time; note that the resistivity of the solution is 10 Ω m in this case. The anisotropic resistivities are basically stable after 6 days. Fig. 7(b) shows the influence of the saturated sodium chloride solution on the anisotropic resistivities. It is obvious that the vertical and horizontal resistivities vary monotonically with the solution resistivity (R_{so}).

3.3.2. Physical construction

In the physical simulation, five anisotropic formation models with different resistivities and dipping angles are constructed and

tested. The specific model parameters are shown in Table 2.

The ranges of the saturated solution resistivity, horizontal resistivity and vertical resistivity are 5.2−11.1 Ω m, 14.8−28.6 Ω m and 149.6−274.5 Ω m, respectively. To ensure the suitability of the anisotropic equivalent medium, the maximum thickness of the saturated board medium and the variable resistivity solution can be determined according to the longitudinal resolution of the instrument. The physical formation model is shown in Fig. 8. Note that the model with a dipping angle (θ) of 90° can be replaced by adjusting the resistivity to obtain a model with an angle of 0°.

3.4. Half-space method

In this section, the half-space measurement method, in which half of the instrument surface is placed in air horizontally so that the upper boundary of the formation model is flush with the interface of the resistivity solution, is introduced to save space and simplify operations, as shown in Fig. 2(b). To verify the reasonability of adopting this scheme, the electric field distribution of the full-space model is analyzed based on *COMSOL*. The 3D formation model is shown in Fig. 9(a). This model is designed as follows: the diameter of the borehole *rb* is 8 in, the resistivity of the mud filtrate *Rm* is 0.1 Ω m, the dipping angle θ is 30°, the resistivity of the surrounding bed *Rs* is 2 Ω m, the thickness of the middle layer *H* is 5 m, and the horizontal and vertical resistivities are 10 Ω m and 20 Ω m, respectively. Here, the electric field generated by the shallow detection mode (*RLA*1) is chosen as an example to analyze the efficiency of the half-space measurement approach. When the measurement point of the instrument is located at the center of the anisotropic layer, the electric field at $x = 0$ is shown in Fig. 9(b). The electric field distribution in this direction is symmetrical, which supports the feasibility of the half-space measurement approach. In addition, the characteristics of the electric field at $y = 0$ are exactly the same as those in Fig. 9(b).

Then, the half-space measurement method is applied to physical simulations process and compared the results with those of the full-space method (the instrument was immersed in sodium chloride solution). The model parameters and measurement results are shown in Table 3. The resistivities of Models 1 to 4 are 8 Ω m, 22 Ω m, 45 Ω m and 103 Ω m, and the ambient temperatures are 18.63 °C, 21.81 °C, 18.63 °C and 19.75 °C, respectively.

Table 3 shows that although the results obtained with the full-space method can represent the true formation resistivity, the half-space results are approximately 1.86 times larger, which indicates that the measuring results are almost not affected by the surrounding environment and can be converted to full-space values, i.e., the measurement accuracy can be guaranteed. In addition, compared with the full-space method, this novel experimental method can reduce the amount of sodium chloride solution required, and it is convenient for operation, experimental measurement and maintenance of experimental equipment.

4. Result

4.1. Physical simulation results

The implementation details of the physical simulation scheme based on the downscaled instrument and formation module are presented. Due to the low resistivity and small anisotropy
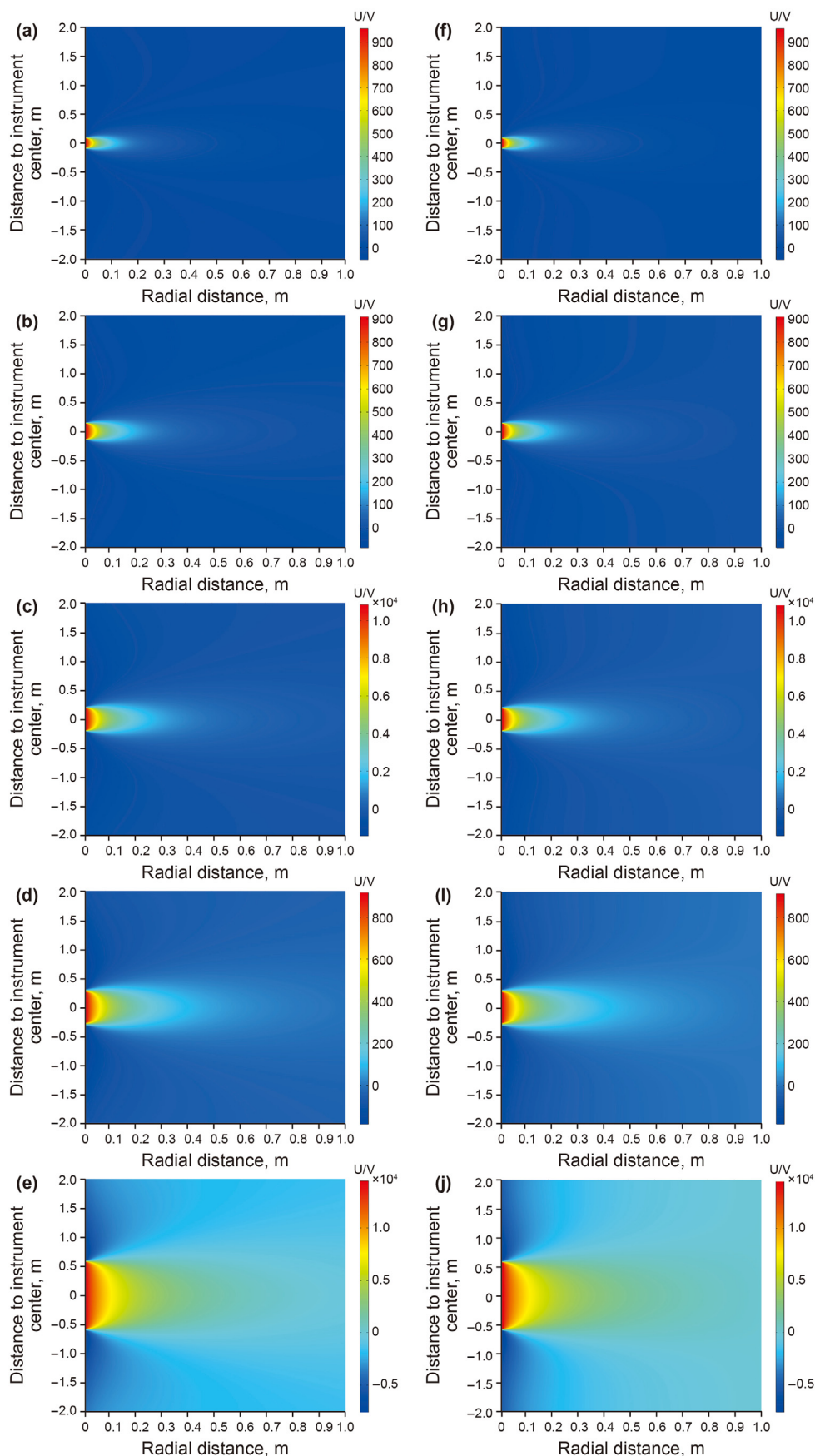
Fig. 4. Electric field distributions for the downscaled instrument (the center of the instrument is at the origin; the distance is positive when the measurement point is above the center point and negative when it is below the center point): (a)–(e) E_{RLA1}–E_{RLA5}; (f)–(j) $E_{RLA1'}$–$E_{RLA5'}$.
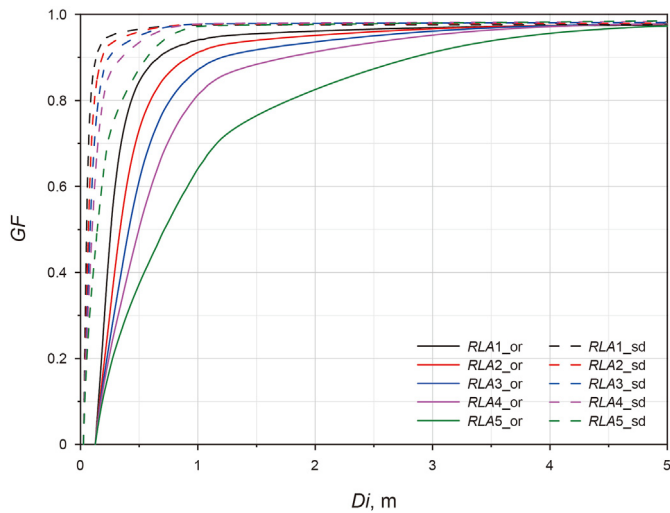
Fig. 5. Pseudo-geometric factor comparison between the original and downscaled instruments.

Table 2
Parameters of the anisotropic formation models.

Model number	1	2	3	4	5
Dipping angle, °	0	30	45	60	90
R_{so}, Ω·m	11.1	8	10.1	5.2	10.2
R_h, Ω·m	25.8	28.6	22.9	14.8	25.1
R_v, Ω·m	260.5	274.5	225.8	149.6	253.4

coefficient of the thin interbedding sand-mudstone formation, the horizontal resistivity range of the formation model used in the physical experiment is designed to be 10-200 Ω-m, and the anisotropy coefficient range is 1–3. The five downscaled formation models used in the physical simulation were designed as follows: borehole diameter $rb = 6$ cm; dipping angles $\theta = 0°$, 30°, 45°, 60° and 90°; and apparent thickness $H = 1.2$ m, 1.38 m, 1.7 m, 2.0 m and 1.2 m. To stabilize the anisotropic resistivities, the model was immersed in a water tank filled with sodium chloride solution for 6 days to fully saturate the anisotropic formation model, and the horizontal and vertical resistivity of the soaked model was sampled, measured and recorded. The resistivity distribution is shown in Table 2. Then, the model is placed at a predetermined
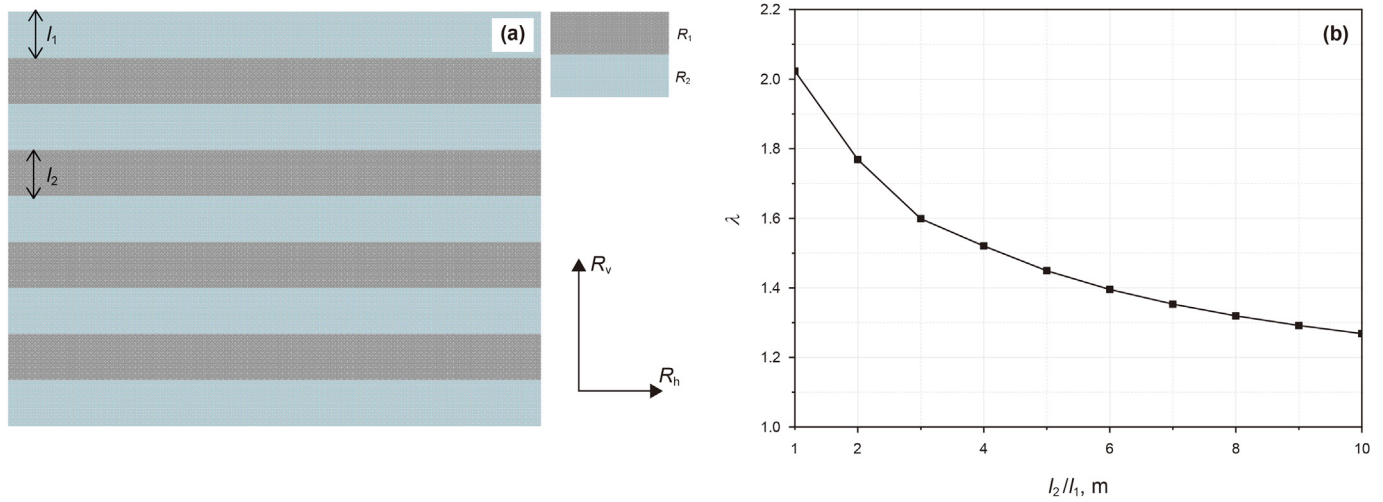

Fig. 6. Anisotropic model: (a) thinly interbedded model; (b) anisotropy coefficient variations with the relative thickness.
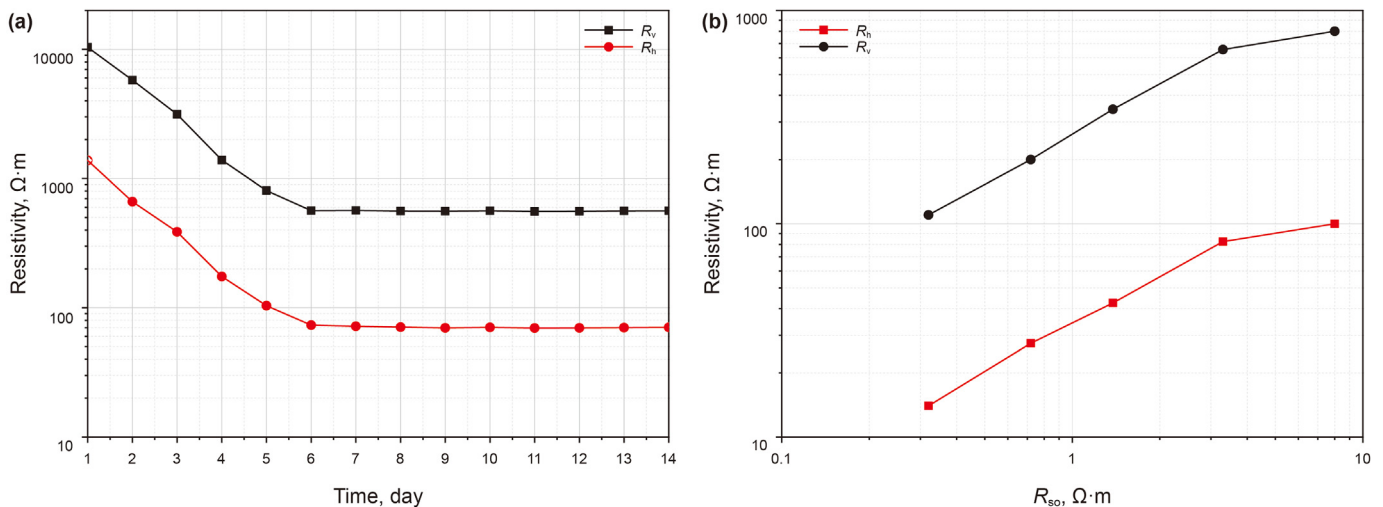

Fig. 7. Variations in anisotropic resistivity with (a) saturation time and (b) solution resistivity.

Fig. 8. Formation models with different dipping angles: (a) $\theta = 0°$; (b) $\theta = 30°$; (c) $\theta = 45°$ and (d) $\theta = 60°$.
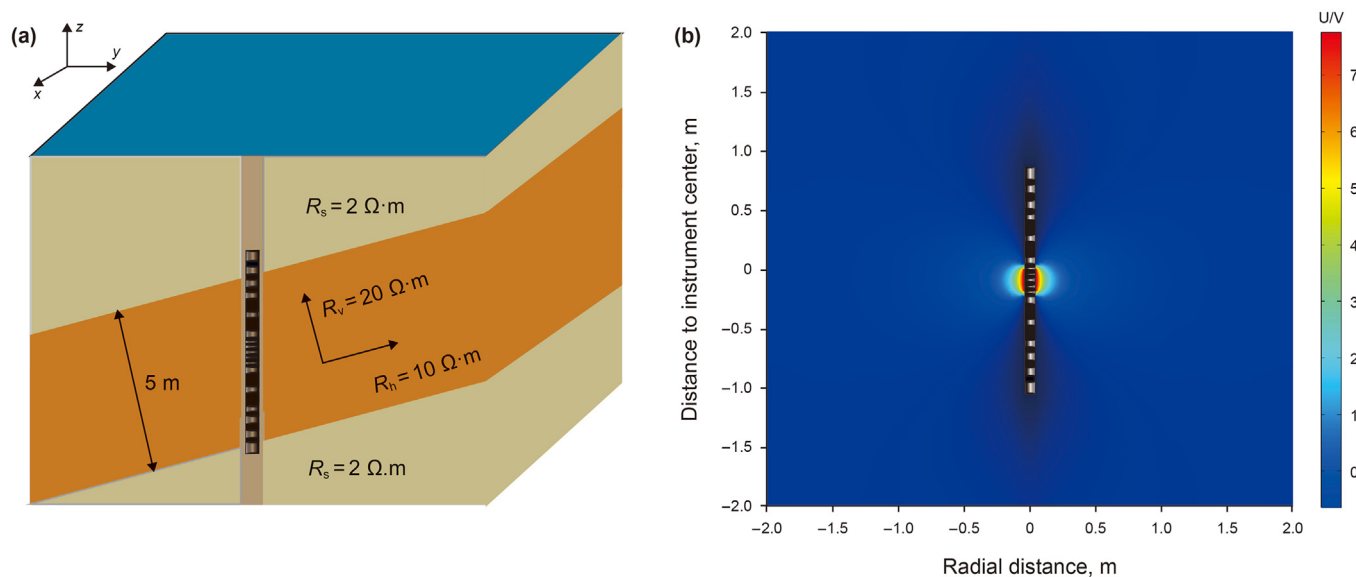

Fig. 9. Electric field distribution for the 3D model: (a) 3D anisotropic formation model and (b) electric field generated by $RLA1$ ($x = 0$).

Table 3
Half space measurement results.

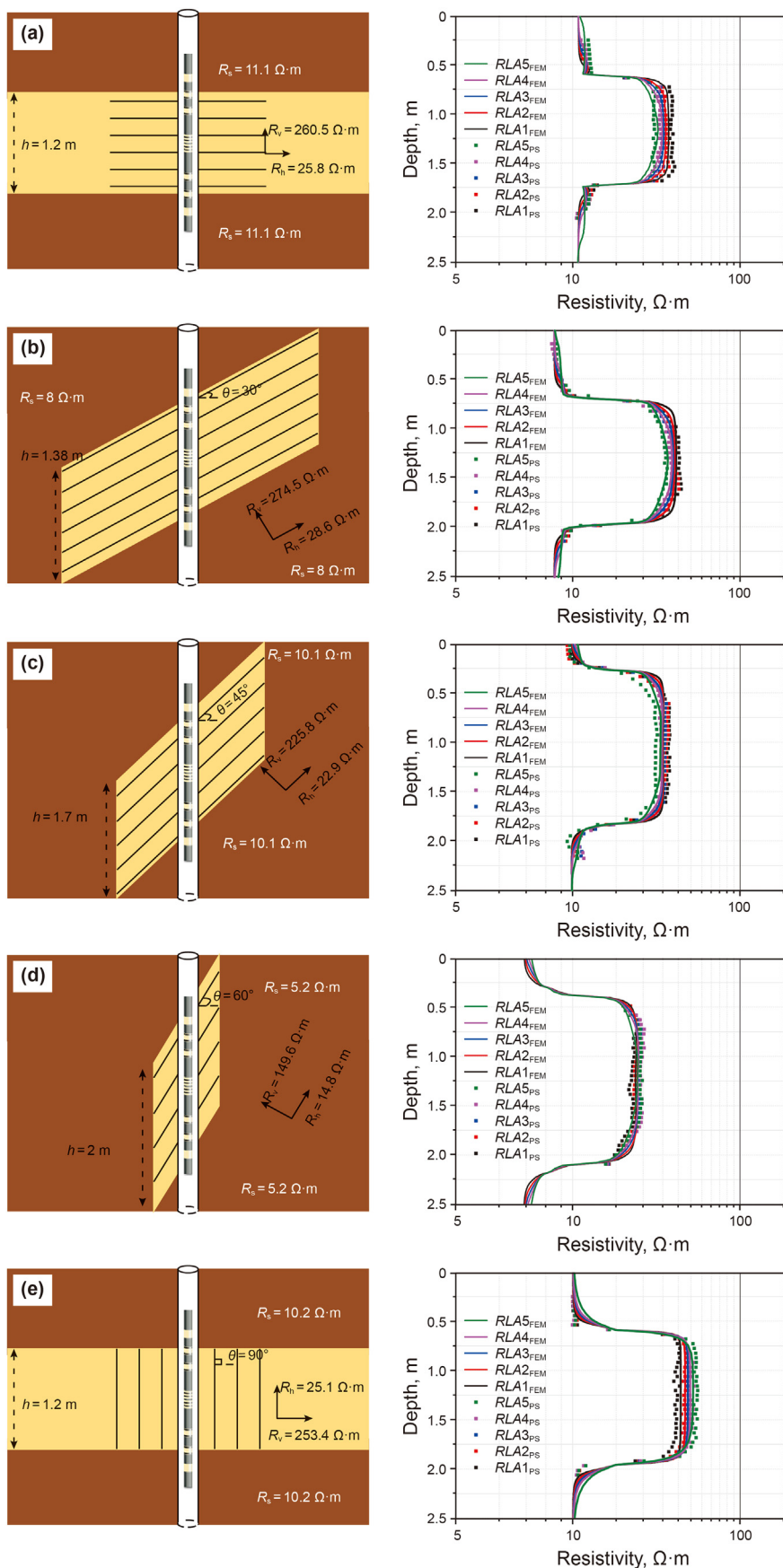| Test model		Detection mode				
		$RLA1$, $\Omega \cdot m$	$RLA2$, $\Omega \cdot m$	$RLA3$, $\Omega \cdot m$	$RLA4$, $\Omega \cdot m$	$RLA5$, $\Omega \cdot m$
Model 1	Full/half-space	7.81/14.63	7.89/14.77	7.88/14.76	7.69/14.30	7.89/14.78
Model 2	Full/half-space	21.54/40.16	21.77/40.49	21.78/40.54	21.27/39.57	21.90/40.80
Model 3	Full/half-space	44.20/82.21	44.71/83.16	44.77/83.27	43.76/81.39	45.21/84.09
Model 4	Full/half-space	101.62/189.02	102.95/191.52	103.23/192.11	101.09/188.03	104.88/196.12

Fig. 10. Comparison between the results of the physical and numerical simulations with the deviated anisotropic model: (a) 0°, (b) 30°, (c) 45°, (d) 60°, and (e) 90°.

Table 4
Relative errors under different dipping angles.

Dipping angle	Anisotropy coefficient	Relative error					MRE
		RLA1	RLA2	RLA3	RLA4	RLA5	
0°	3.18	1.27%	0.04%	2.68%	3.77%	4.23%	2.40%
30°	3.10	4.01%	1.43%	1.34%	3.68%	3.53%	2.80%
45°	3.14	6.93%	3.82%	1.89%	0.71%	6.88%	4.05%
60°	3.18	7.20%	3.32%	0.09%	3.10%	2.50%	3.24%
90°	3.18	6.82%	0.45%	2.67%	1.99%	7.16%	3.82%

location to make measurements. The downscaled instrument is positioned in the center of the borehole by adjusting the length of the bracket, and then the operator could control the downscaled instrument and move it forward at a constant speed with a step motor. The computer terminal on the ground automatically received the measurement signal. To eliminate the influence of liquid level fluctuations on the signal, the forward speed of the instrument was empirically set to 0.2 m/min.

Based on the determined scaling instrument and experimental model parameters, the physical (RLA_{PS}) simulation results are compared with the numerical (RLA_{FEM}) simulation results in Fig. 10.

The figure shows that (1) the amplitudes of the five curves increase as the measurement point gradually enters the high-resistivity

layer; (2) when the measurement point is located in the high-resistivity layer, a negative or positive difference phenomenon is observed, as shown in Fig. 10(a)–(c) or Fig. 10(d) and (e); i.e., $RLA5<RLA4<RLA3<RLA2<RLA1$ or $RLA5 > RLA4>RLA3>RLA2>RLA1$; (3) due to the influence of anisotropy, the response value is larger than the horizontal resistivity; and (4) when the measurement point is far from the high-resistivity layer, the amplitudes of curves for different $DoIs$ rapidly decrease.

In addition, Table 4 shows the relative error and mean relative error (MRE) between the numerical simulation (RLA_{FEM}) and physical simulation (RLA_{PS}) responses when the measurement point is located at the center of the formation model. The relative errors range from 0.04% to 7.2%, and the maximum MRE is less than
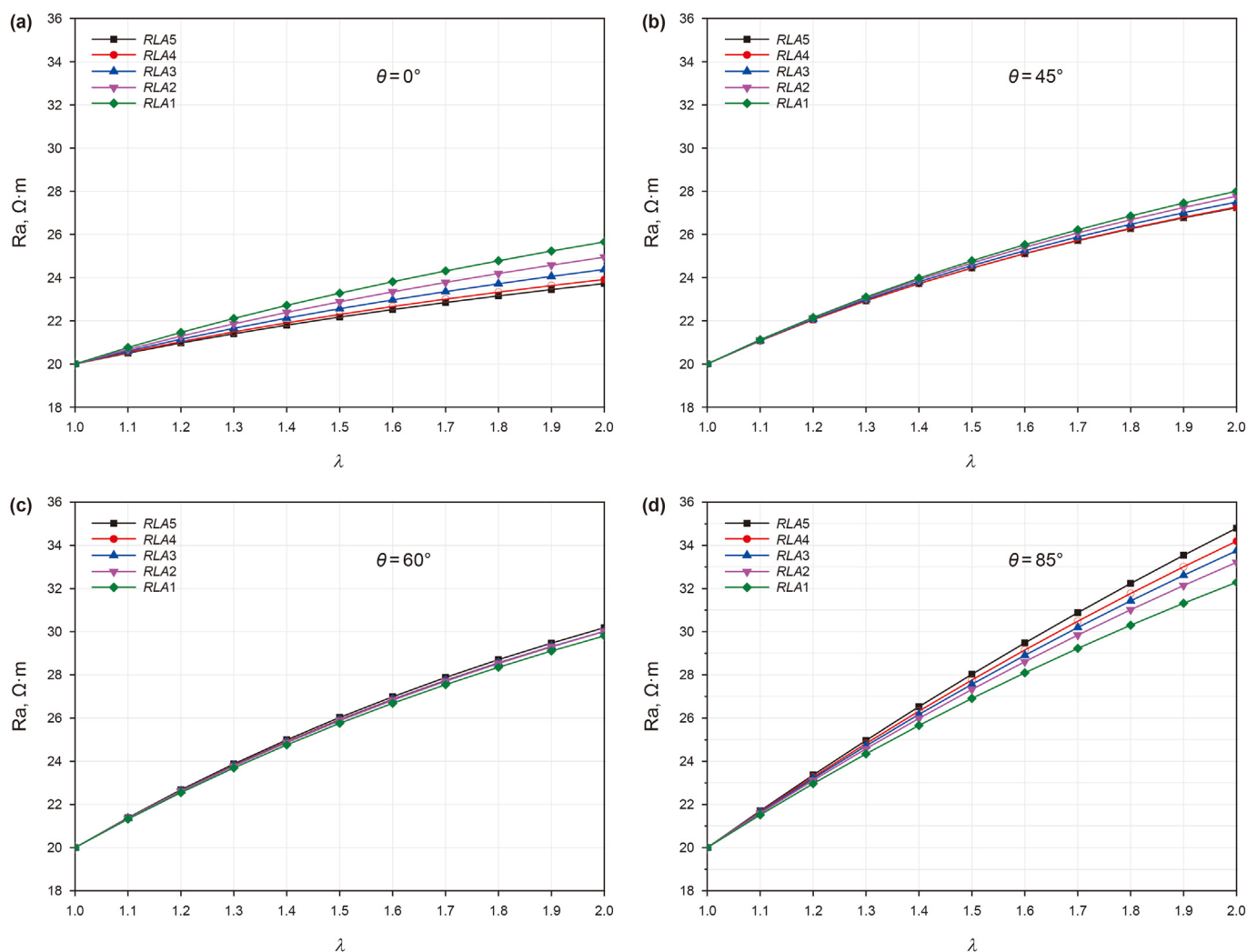

Fig. 11. The effects of anisotropy and dipping angle on array laterolog responses: (a) $\theta = 0°$; (b) $\theta = 45°$; (c) $\theta = 60°$ and (d) $\theta = 85°$.
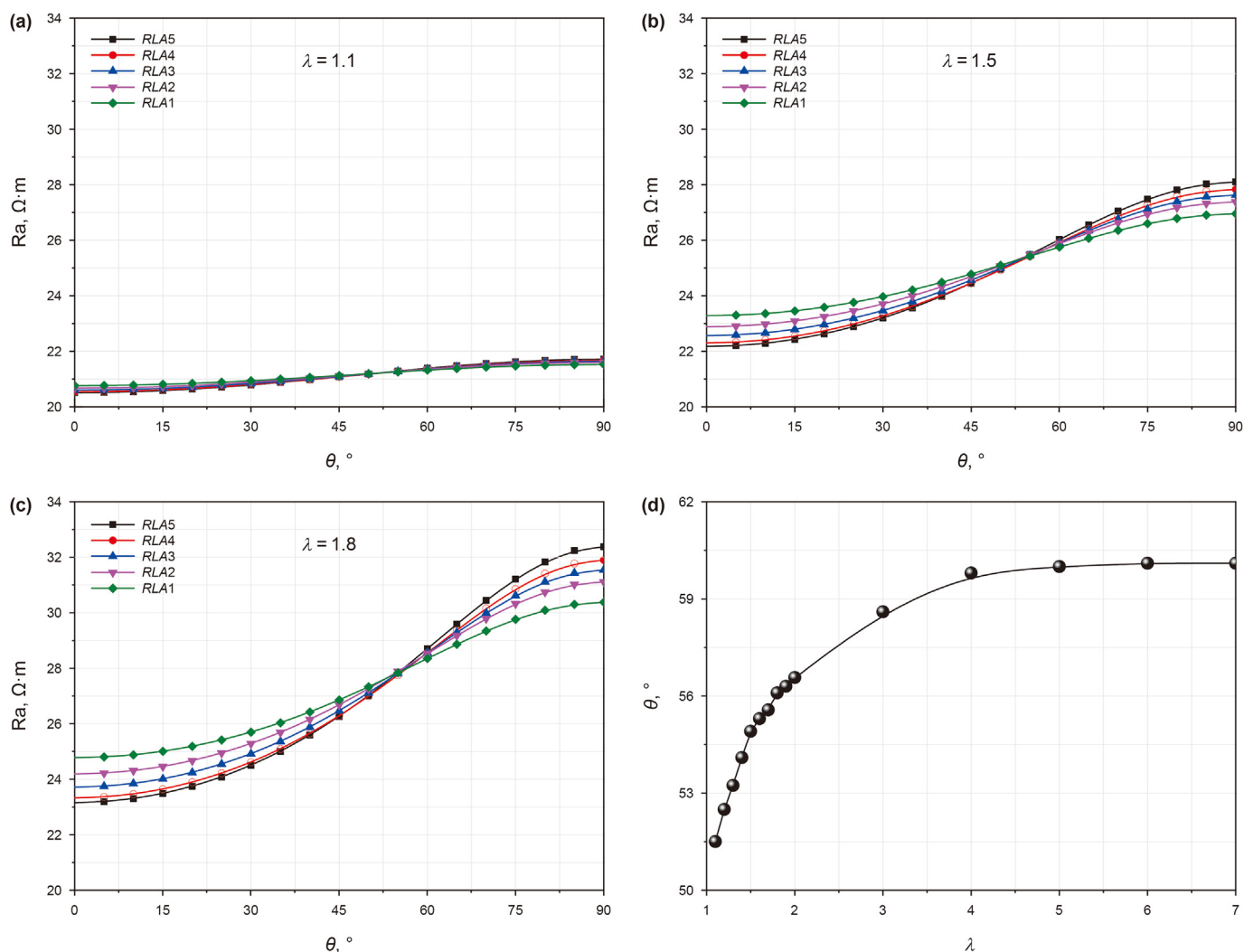
Fig. 12. The reversal characteristics of the array laterolog response curves: (a) $\lambda = 1.1$; (b) $\lambda = 1.5$; (c) $\lambda = 1.8$ and (d) the range of reversal angle.

5%, which verifies the accuracy of the numerical simulation algorithm.

Based on the description of the physical simulation above, the numerical simulation algorithm is verified; moreover, a lateral physical simulation platform for relatively systematic arrays is established. The proposed approach can significantly improve the physical simulation technology used in the field of direct current (DC) electric logging and provide a new scheme for the construction of other physical simulation platforms.

4.2. Numerical simulation results

To investigate the responses characteristics of the array laterolog, Fig. 11 shows the responses in homogeneous anisotropic formations with different anisotropy coefficients λ. From Fig. 11(a)−(d), the dipping angles are $0°$, $45°$, $60°$ and $85°$. The range of anisotropy coefficients is from 1 to 2.

In Fig. 11, the curves gradually separate as the anisotropy coefficient increases. The larger λ is, the larger the degree of separation. Furthermore, the five curves exhibit a negative anomaly at low dipping angles, e.g., $0°$ and $45°$. However, the curves reverse and display a positive anomaly when the dipping angle increases; this finding is consistent with the results of the physical simulation.

To get the more information of the reversal, three anisotropic

formation models are adopted, and the anisotropy coefficients are 1.1, 1.5 and 1.8. The borehole diameter is 8 in, and the mud has a resistivity of $0.1\ \Omega\cdot m$. The horizontal resistivity R_h is $20\ \Omega\cdot m$. The dipping angle varies from $0°$ to $90°$. The responses of the array laterolog are shown in Fig. 12(a)-(c).

The five curves gradually transition from showing a negative difference to showing a positive difference as the dipping angle increases. As the dipping angle increases, the apparent resistivities of the curves also increase, and the growth rates are as follows: $RLA1>RLA2>RLA3>RLA4>RLA5$. Furthermore, the larger the anisotropy coefficient is, the greater the curve separation, and the more obvious the curve reversal. By identifying the reversal angles associated with different anisotropy coefficients, as shown in Fig. 12(d), the reversal angle reaches a plateau when the anisotropy coefficient is larger than 5. Numerous numerical simulation results show that the reversal angle ranges from $50°$ to $62°$. The existence of a reversal angle can explain the variations in array laterolog responses.

5. Discussion

5.1. Effects of anisotropy and dipping angle

To analyze the sensitivity of array laterolog responses to the formation anisotropy coefficient and dipping angle, the sensitivity
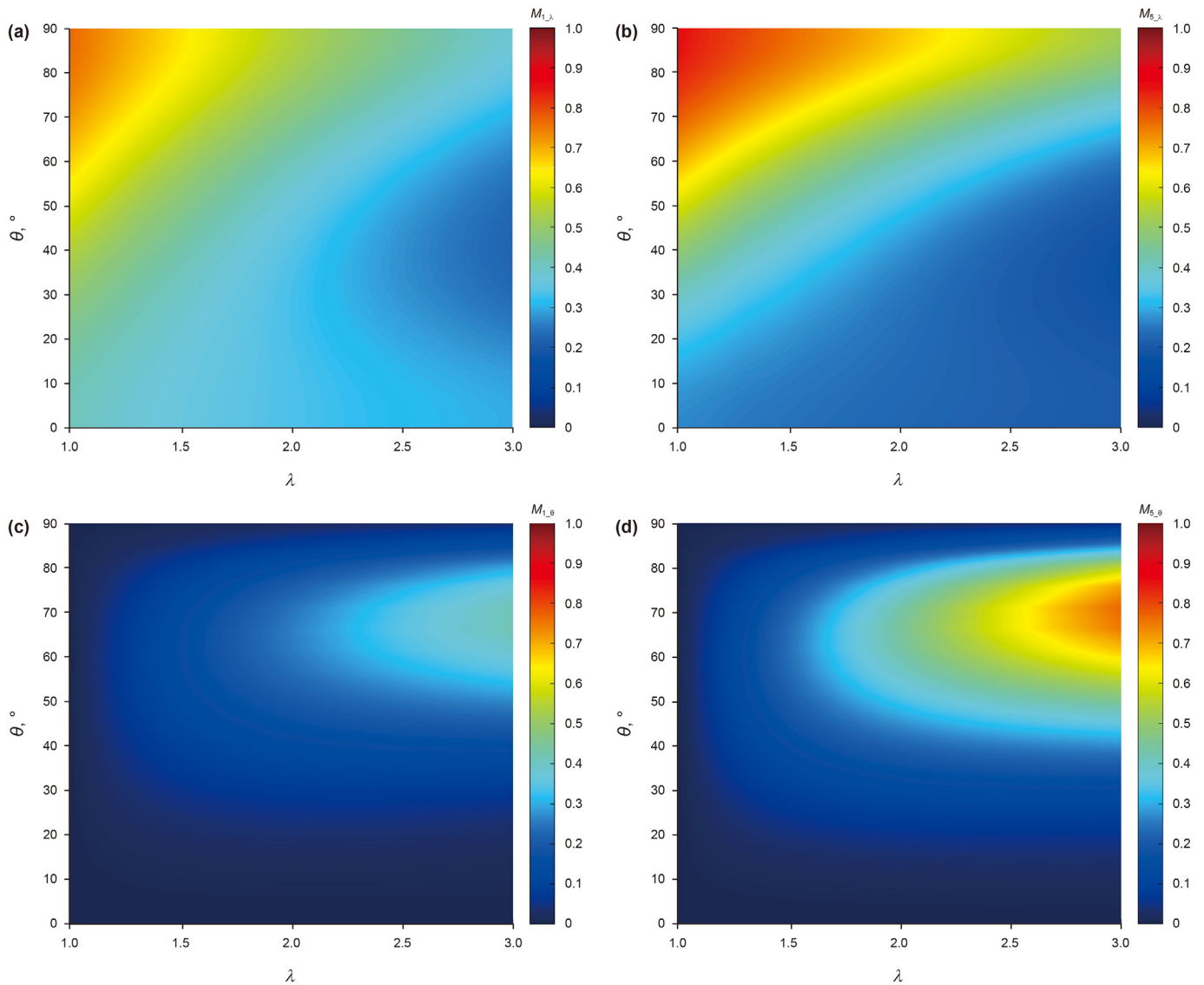
Fig. 13. Distributions of sensitivity functions: (a)$\partial RLA1/\partial \lambda$; (b) $\partial RLA5/\partial \lambda$; (c) $\partial RLA1/\partial \theta$ and (d) $\partial RLA5/\partial \theta$

function is defined as:

$$M_i = \frac{\partial RLAi}{\partial x}, x = \lambda, \theta;\ i = 1, \cdots, 5 \tag{8}$$

where i is the detection mode of the array laterolog and x is a parameter of the formation model.

Taking $RLA1$ and $RLA5$ as examples, Fig. 13(a)-(b) and Fig. 13(c)–(d) show the distributions of sensitivity functions for the anisotropy coefficient and dipping angle, respectively. The borehole diameter is 8 in, and the mud has a resistivity of 0.1 Ω·m. The horizontal resistivity R_h is 20 Ω·m. The ranges of the anisotropy coefficient and dipping angle are 1−3 and 0°−90°, respectively.

Notably, (1) the responses of the array laterolog are most sensitive to anisotropy at high dipping angles (60°−90°), and the greater *DoI* is, the more sensitive the detection mode is to anisotropy; (2) the responses of the array laterolog are most sensitive to the dipping angle at angles from 50° to 80°, and the greater *DoI* is, the more sensitive the detection mode is to the dipping angle.

In addition, to quantitatively analyze the effects of parameters on the responses of the array laterolog, the separation factor and

amplitude variation of the curves are defined as shown in Eqs. (9) and (10), respectively.

$$F = \frac{\max\{RLA1, RLA2, RLA3, RLA4, RLA5\}}{\min\{RLA1, RLA2, RLA3, RLA4, RLA5\}} \tag{9}$$

$$U_i = \frac{RLAi - R_t}{R_t} \times 100\%,\ i = 1, \cdots, 5 \tag{10}$$

where $RLA1-RLA5$ are the apparent resistivities of the five detection modes.

For instance, the separation factors of the curves with 0° dipping angle in Fig. 11 are shown in Table 5. The larger λ or θ is, the larger the amplitudes of the curves. Specifically, compared to the lowest result, U_5, the amplitude of $RLA5$, will increase by 74.0% when λ and θ are 2 and 85°, respectively. Therefore, the responses of the array laterolog are similar to the horizontal resistivity results at low dipping angles and are sensitive to anisotropy in formations with high dipping angles.

In addition, from the distribution of the sensitivity function, the

Table 5
Separation factors for different λ values when $\theta = 0°$.

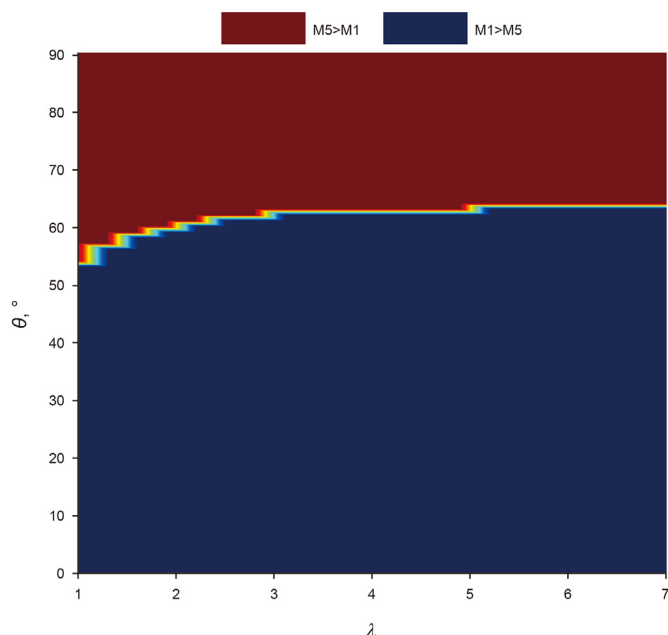| λ	0	1.2	1.4	1.6	1.8	2.0
F	1.00	1.02	1.04	1.06	1.07	1.08

Fig. 14. The sensitivity of the reversal angle to anisotropy.

rationality of the reverse phenomenon in Fig. 11 can be illustrated. The responses of the array laterolog become increasingly sensitive to formation anisotropy as the dipping angle increases, and the sensitivity of a curve with a deep *DoI* to formation anisotropy is greater than that for a curve with a shallow *DoI*. Therefore, compared with the shallow detection curve, the deep detection curve is closer to the vertical resistivity, which leading to the reverse phenomenon of array laterolog response curves.

5.2. Reversal angle

From Sec. 5.1, it is obvious that to determine the interval of the curve reversal angle in deviated anisotropic formations, the cases in which the sensitivity of *RLA*5 to anisotropy is greater than that of *RLA*1 should be specified. Therefore, the sensitivity functions M5 and M1 are subtracted to obtain the angle range, as shown in Fig. 14. The red area in the figure indicates that M5>M1, i.e., *RLA*5 is more sensitive to anisotropy than *RLA*1, which means that *RLA*5 mainly reflects the vertical resistivity of the formation, and $RLA5 > RLA1$. The blue area indicates that M5<M1, i.e., *RLA*5 is less sensitive to anisotropy than *RLA*1, which means that $RLA1 > RLA5$.

With increasing dipping angle, the sensitivity relationship is gradually reversed, which causes the array laterolog response curves to also reverse. The critical angle of sensitivity inversion is located between $50°$ and $70°$. Therefore, in deviated anisotropic formations, the reversal angle of the array laterolog curves should be between $50°$ and $70°$, which is consistent with the numerical modeling results and make a reasonable explanation for the existence of the reversal angle.

6. Conclusion

3D-FEM modeling and physical simulation schemes for array

laterolog responses in deviated anisotropic formations are presented in this paper. The experimental scheme can be extended flexibly by readers if more complex geological models are encountered in practice. By analyzing the results of numerical and physical simulations at different dipping angles and anisotropic coefficients, the following conclusions are obtained:

(1) The physical simulation system for array laterolog mainly includes a downscaled instrument module, a downscaled formation module, a measurement module and a post-processing module.
(2) The horizontal and vertical downscaling ratios of the experimental instrument are determined to be 1/3 and 1/6, respectively, and the length, width, and height of the downscaled formation module are determined to be 4 m, 2 m and 2 m, respectively, based on the implementation of truncated boundaries.
(3) A thin interbedded plank formation, which is saturated with a sodium chloride solution, is used as an equivalent to the downscaled formation model; additionally, the half-space measurement method can greatly improve the experimental efficiency, and a high measurement accuracy can be guaranteed.
(4) The *MRE* between the physical and numerical simulation results ranges from 2.40% to 4.05%, thus verifying the accuracy of the numerical simulation method.
(5) Changing the anisotropy coefficient can make curves with different *DoIs* increase and separate from each other, and the larger the anisotropy coefficient is, the faster the increase and separation processes; changing the dipping angle causes the curves with different *DoIs* to gradually transition from showing a negative difference to showing a positive difference, and the corresponding range of the reversal angle is from $50°$ to $62°$.
(6) A sensitivity function is established to explain the existence of the reversal angle, and this approach provides a novel perspective for processing array laterolog data.

Acknowledgements

References

Attila, G., Mátyás, H., Dezső, D., et al., 2016. Effect of the eccentricity of normal resistivity borehole instruments on the current field and resistivity measurement. J. Appl. Geophy. 4 (134), 281–290. https://doi.org/10.1016/j.jappgeo.2016.09.001.

Chen, H., 2009. Study and Application of Array Laterolog Inversion Method. School of Geosciences in China University of Petroleum (East China), Qingdao (in Chinese).

Deng, S.G., Tong, Z.Q., Fan, Y.R., 2006. Numerical simulation of dual laterolog response in tilted anisotropic formation. Acta Pet. Sin. 27 (3), 61–64. https://doi.org/10.7623/syxb200603013 (in Chinese).

Deng, S.G., Li, Z.Q., Fan, Y.R., et al., 2010. Numerical simulation of mud invasion and its array laterolog response in deviated well. Chin. J. Geophys. 53, 994–1000. https://doi.org/10.1002/cjg2.1496, 04, (in Chinese).

Frenkel, M.A., Geldmacher, I.M., Georgi, D.T., et al., 2000. Application of array resistivity measurements in horizontal wells. Lead. Edge 19 (4), 179–192. https://doi.org/10.2118/62913-MS.

Fan, Y.R., Hu, X.F., Deng, S.G., et al., 2019. Logging while drilling electromagnetic wave responses in inclined bedding formation. Petrol. Explor. Dev. 46 (4), 675–683. https://doi.org/10.1016/S1876-3804(19)60228-4.

Fan, Y.R., Wang, L., Ge, X.M., et al., 2016. Response simulation and corresponding analysis of dual laterolog in cavernous reservoirs. Petrol. Explor. Dev. 43 (2), 237–243. https://doi.org/10.1016/S1876-3804(16)30029-5.

Griffiths, R., Barber, T., Faivre, O., et al., 2000. Optimal evaluation of formation

resistivities using array induction and array laterolog instruments. In: SPWLA 41th Annual Logging Symposium, 4–7 June 2000, Dallas, Texas.

Ge, X.M., Fan, Y.R., Li, J., et al., 2019. Experimental studies and investigations on the dual laterolog responses of near borehole fracture. Chin. J. Geophys. 62 (1), 61–67. https://doi.org/10.6038/cjg2018L0128 (in Chinese).

Hu, S., Li, J., Guo, H.B., et al., 2017. Analysis and application of the response characteristics of DLL and LWD resistivity in horizontal well. Appl. Geophys. 14 (3), 351–362. https://doi.org/10.1007/s11770-017-0635-8.

Hu, X.F., Fan, Y.R., 2018. Huber inversion for logging-while-drilling resistivity measurements in high angle and horizontal wells. Geophysics 83 (4), D113–D125. https://doi.org/10.1190/geo2017-0459.1.

Itskovich, G.B., Mezzatesta, A.G., Strack, K.M., et al., 1998. High-definition lateral log - resistivity device: basic physics and resolution. In: SPWLA 39th Annual Logging Symposium, 26–28 May 1998, Keystone, Colorado.

Isabelle, D., Richard, L., Martin, G.L., 2017. The paradox of anisotropy and the array-laterolog anisotropy response. In: SPWLA 58th Annual Logging Symposium, 17–21 June 2017, Oklahoma City, Oklahoma, USA.

Jiang, H.Q., Ye, S.Y., Lei, Z.X., et al., 2010. The productivity evaluation model and its application for finite conductivity horizontal wells in fault block reservoirs. Petrol. Sci. 7 (4), 530–535. https://doi.org/10.1007/s12182-010-0104-y.

Jadwiga, A.J., Adam, C., Dezso, D., et al., 2016. New methods for modeling laterolog resistivity corrections. Acta Geophys. 64 (2), 417–442. https://doi.org/10.1515/acgeo-2016-0012.

Ke, S.Z., Feng, Q.N., Shang, Z.Y., 1996. Experimental instrument for physical analogy of dual laterolog. Well Logging Technol. 20 (4), 282–286. https://doi.org/10.16489/j.issn.1004-1338.1996.04.010 (in Chinese).

Ke, S.Z., Feng, Q.N., Shang, Z.Y., 2003. On scale modeling of dual laterolog responses to fractured formation. Well Logging Technol. 27 (5), 253–355. https://doi.org/10.3969/j.issn.1004-1338.2003.05.001 (in Chinese).

Li, H., Wang, L., 2019. Fast Modeling and practical inversion of laterolog-type downhole resistivity measurements. IEEE Trans. Geosci. Rem. Sens. 57 (1), 120–127. https://doi.org/10.1109/tgrs.2018.2852608.

Maurer, H., Antonov, Y., Corley, Y., et al., 2009. Advanced processing for a new array laterolog instrument. In: SPWLA 50th Annual Logging Symposium, 21–24 June 2009. The Woodlands, Texas.

Ollivier, F., Tom, B., Lauret, J., et al., 2002. Using array induction and array laterolog data to characterize resistivity anisotropy in vertical wells. In: SPWLA 43th Annual Logging Symposium, 2–5 June 2002. Oiso, Japan.

Smits, J.W., Dubourg, I., Luling, M.G., et al., 1998. Improved resistivity interpretation utilizing a new array laterolog instrument and associated inversion processing. In: 1998 SPE Annual Technical Conference and Exhibition, 27-30 September 1998, New Orleans, Louisiana.

Wu, J.C., Fan, Y.R., Wu, F., et al., 2019a. Combining large-sized model flow experiment and NMR measurement to investigate drilling induced formation damage in sandstone reservoir. J. Petrol. Sci. Eng. 17 (4), 577–581. https://doi.org/10.1016/j.petrol.2019.01.005.

Wu, Z.G., Deng, S.G., Xu, Q.H., et al., 2020. Numerical simulation and dimension scale-down analysis of electromagnetic logging while drilling of horizontal wells in complex structures. Petrol. Sci. 17 (4), 645–657. https://doi.org/10.1007/s12182-020-00444-y.

Wang, T., Xiao, L., Mezzatesta, A., 1999. Array laterolog and dual laterolog resistivity measurements in horizontal wells: a comparative model study. In: 1999 SEG Annual Meeting, 31 October–5 November, Houston, Texas.

Wu, Z.G., Fan, Y.R., Wang, J.W., et al., 2019b. Application of 2.5-D finite difference method in logging-while-drilling electromagnetic measurements for complex scenarios. Geosci. Rem. Sens. Lett. IEEE 17 (4), 577–581. https://doi.org/10.1109/lgrs.2019.2926740.

Xia, P., Liu, D.R., Wan, W.C., et al., 2011. Numerical simulation of dual laterolog response in horizontal anisotropic formation. J. Oil Gas Technol. (J. Jianghan Petroleum Inst.) 33 (8), 104–108. https://doi.org/10.3969/j.issn.1000-9752.2011.08.023 (in Chinese).

Yuan, C., Li, C.L., Zhou, C.C., 2020. Forward simulation of array laterolog resistivity in anisotropic formation and its application. Petrol. Explor. Dev. 47 (1), 77–85. https://doi.org/10.1016/s1876-3804(20)60007-6.

Yin, C.F., Ke, S.Z., Xu, W., et al., 2014. 3D laterolog array sonde design and response simulation. Appl. Geophys. 11 (2), 223–234. https://doi.org/10.1007/s11770-014-0439-z.

Yuan, X.Y., Deng, S.G., Wang, L., et al., 2018. Numerical and experimental simulations of multiarray azimuthal resistivity laterolog responses in fractured reservoir. In: 2018 SEG International Exposition and Annual Metting, 14-19 October, Anaheim, California, USA.

Zhao, L.X., Bu, Y., 1994. Logging Evaluation of Carbonate Reservoir. Petroleum Industry Press, Beijing (in Chinese).

Zhang, G.J., 2009. Electrical Logging Algorithm. Petroleum Industry Press, Beijing (in Chinese).

Zhu, P., Li, Z.Q., Chen, M., et al., 2019. Study on forward and inversion modeling of array laterolog logging in a horizontal/highly deviated well. Acta Geophys. 67 (5), 1307–1318. https://doi.org/10.1007/s11600-019-00321-2.